The Astrophysical Journal, 943:129 (10pp), 2023 February 1 https://doi.org/10.3847/1538-4357/acae88

Polarization Properties of the Weakly Magnetized Neutron Star X-Ray Binary GS 1826–238 in the High Soft State

Fiamma Capitanio[1], Sergio Fabiani[1], Andrea Gnarini[2], Francesco Ursini[2], Carlo Ferrigno[3], Giorgio Matt[2], Juri Poutanen[4,5], Massimo Cocchi[6], Romana Mikusincova[2], Ruben Farinelli[7], Stefano Bianchi[2], Jari J. E. Kajava[4,8], Fabio Muleri[1], Celia Sanchez-Fernandez[9], Paolo Soffitta[1], Kinwah Wu[10], Iván Agudo[11], Lucio A. Antonelli[12,13], Matteo Bachetti[6], Luca Baldini[14,15], Wayne H. Baumgartner[16], Ronaldo Bellazzini[14], Stephen D. Bongiorno[16], Raffaella Bonino[17,18], Alessandro Brez[14], Niccolò Bucciantini[19,20,21], Simone Castellano[14], Elisabetta Cavazzuti[22], Stefano Ciprini[13,23], Enrico Costa[1], Alessandra De Rosa[1], Ettore Del Monte[1], Laura Di Gesu[22], Niccolò Di Lalla[24], Alessandro Di Marco[1], Immacolata Donnarumma[22], Victor Doroshenko[25], Michal Dovčiak[26], Steven R. Ehlert[16], Teruaki Enoto[27], Yuri Evangelista[1], Riccardo Ferrazzoli[1], Javier A. Garcia[28], Shuichi Gunji[29], Kiyoshi Hayashida[30,51], Jeremy Heyl[31], Wataru Iwakiri[32], Svetlana G. Jorstad[33,34], Vladimir Karas[26], Takao Kitaguchi[27], Jeffery J. Kolodziejczak[16], Henric Krawczynski[35], Fabio La Monaca[1], Luca Latronico[17], Ioannis Liodakis[36], Simone Maldera[17], Alberto Manfreda[14], Frédéric Marin[37], Andrea Marinucci[22], Alan P. Marscher[33], Herman L. Marshall[38], Ikuyuki Mitsuishi[39], Tsunefumi Mizuno[40], C.-Y. Ng[41], Stephen L. O'Dell[16], Nicola Omodei[24], Chiara Oppedisano[17], Alessandro Papitto[12], George G. Pavlov[42], Abel L. Peirson[24], Matteo Perri[12,13], Melissa Pesce-Rollins[14], Pierre-Olivier Petrucci[43], Maura Pilia[6], Andrea Possenti[6], Simonetta Puccetti[13], Brian D. Ramsey[16], John Rankin[1], Ajay Ratheesh[1], Roger W. Romani[24], Carmelo Sgrò[14], Patrick Slane[44], Gloria Spandre[14], Toru Tamagawa[27], Fabrizio Tavecchio[45], Roberto Taverna[46], Yuzuru Tawara[39], Allyn F. Tennant[16], Nicholas E. Thomas[16], Francesco Tombesi[23,47,48], Alessio Trois[6], Sergey S. Tsygankov[4,5], Roberto Turolla[10,46], Jacco Vink[49], Martin C. Weisskopf[16], Fei Xie[1,50], and Silvia Zane[10]

[1] INAF Istituto di Astrofisica e Planetologia Spaziali, Via del Fosso del Cavaliere 100, I-00133 Roma, Italy; fiamma.capitanio@inaf.it
[2] Dipartimento di Matematica e Fisica, Università degli Studi Roma Tre, Via della Vasca Navale 84, I-00146 Roma, Italy
[3] Department of Astronomy, University of Geneva, Ch. d'Ecogia 16, 1290, Versoix, Geneva, Switzerland
[4] Department of Physics and Astronomy, University of Turku, FI-20014, Finland
[5] Space Research Institute of the Russian Academy of Sciences, Profsoyuznaya Str. 84/32, Moscow 117997, Russia
[6] INAF—Osservatorio Astronomico di Cagliari, via della Scienza 5, I-09047 Selargius (CA), Italy
[7] INAF—Osservatorio di Astrofisica e Scienza dello Spazio di Bologna, Via P. Gobetti 101, I-40129 Bologna, Italy
[8] Aurora Technology for the European Space Agency (ESA), European Space Astronomy Centre (ESAC), Camino Bajo del Castillo s/n, E-28692 Villanueva de la Cañada, Madrid, Spain
[9] ATG Europe for the European Space Agency (ESA), European Space Astronomy Centre (ESAC), Camino Bajo del Castillo s/n, E-28692 Villanueva de la Cañada, Madrid, Spain
[10] Mullard Space Science Laboratory, University College London, Holmbury St Mary, Dorking, Surrey RH5 6NT, UK
[11] Instituto de Astrofísicade Andalucía—CSIC, Glorieta de la Astronomía s/n, E-18008 Granada, Spain
[12] INAF Osservatorio Astronomico di Roma, Via Frascati 33, E-00040 Monte Porzio Catone (RM), Italy
[13] Space Science Data Center, Agenzia Spaziale Italiana, Via del Politecnico snc, I-00133 Roma, Italy
[14] Istituto Nazionale di Fisica Nucleare, Sezione di Pisa, Largo B. Pontecorvo 3, I-56127 Pisa, Italy
[15] Dipartimento di Fisica, Università di Pisa, Largo B. Pontecorvo 3, I-56127 Pisa, Italy
[16] NASA Marshall Space Flight Center, Huntsville, AL 35812, USA
[17] Istituto Nazionale di Fisica Nucleare, Sezione di Torino, Via Pietro Giuria 1, I-10125 Torino, Italy
[18] Dipartimento di Fisica, Università degli Studi di Torino, Via Pietro Giuria 1, I-10125 Torino, Italy
[19] INAF Osservatorio Astrofisico di Arcetri, Largo Enrico Fermi 5, I-50125 Firenze, Italy
[20] Dipartimento di Fisica e Astronomia, Università degli Studi di Firenze, Via Sansone 1, I-50019 Sesto Fiorentino (FI), Italy
[21] Istituto Nazionale di Fisica Nucleare, Sezione di Firenze, Via Sansone 1, I-50019 Sesto Fiorentino (FI), Italy
[22] Agenzia Spaziale Italiana, Via del Politecnico snc, I-00133 Roma, Italy
[23] Istituto Nazionale di Fisica Nucleare, Sezione di Roma "Tor Vergata", Via della Ricerca Scientifica 1, I-00133 Roma, Italy
[24] Department of Physics and Kavli Institute for Particle Astrophysics and Cosmology, Stanford University, Stanford, CA 94305, USA
[25] Institut für Astronomie und Astrophysik, Universität Tübingen, Sand 1, D-72076 Tübingen, Germany
[26] Astronomical Institute of the Czech Academy of Sciences, Boční II 1401/1, 14100 Praha 4, Czech Republic
[27] RIKEN Cluster for Pioneering Research, 2-1 Hirosawa, Wako, Saitama 351-0198, Japan
[28] California Institute of Technology, Pasadena, CA 91125, USA
[29] Yamagata University, 1-4-12 Kojirakawa-machi, Yamagata-shi 990-8560, Japan
[30] Osaka University, 1-1 Yamadaoka, Suita, Osaka 565-0871, Japan
[31] University of British Columbia, Vancouver, BC V6T 1Z4, Canada
[32] Department of Physics, Faculty of Science and Engineering, Chuo University, 1-13-27 Kasuga, Bunkyo-ku, Tokyo 112-8551, Japan
[33] Institute for Astrophysical Research, Boston University, 725 Commonwealth Avenue, Boston, MA 02215, USA
[34] Department of Astrophysics, St. Petersburg State University, Universitetsky pr. 28, Petrodvoretz, 198504 St. Petersburg, Russia
[35] Physics Department and McDonnell Center for the Space Sciences, Washington University in St. Louis, St. Louis, MO 63130, USA
[36] Finnish Centre for Astronomy with ESO, University of Turku, FI-20014 Finland
[37] Observatoire Astronomique de Strasbourg, CNRS, Université de Strasbourg, UMR 7550, F-67000 Strasbourg, France
[38] MIT Kavli Institute for Astrophysics and Space Research, Massachusetts Institute of Technology, 77 Massachusetts Avenue, Cambridge, MA 02139, USA
[39] Graduate School of Science, Division of Particle and Astrophysical Science, Nagoya University, Furo-cho, Chikusa-ku, Nagoya, Aichi 464-8602, Japan
[40] Hiroshima Astrophysical Science Center, Hiroshima University, 1-3-1 Kagamiyama, Higashi-Hiroshima, Hiroshima 739-8526, Japan
[41] Department of Physics, University of Hong Kong, Pokfulam, Hong Kong
[42] Department of Astronomy and Astrophysics, Pennsylvania State University, University Park, PA 16801, USA
[43] Université Grenoble Alpes, CNRS, IPAG, F-38000 Grenoble, France
[44] Center for Astrophysics, Harvard & Smithsonian, 60 Garden Street, Cambridge, MA 02138, USA

[45] INAF Osservatorio Astronomico di Brera, via E. Bianchi 46, I-23807 Merate (LC), Italy
[46] Dipartimento di Fisica e Astronomia, Università degli Studi di Padova, Via Marzolo 8, I-35131 Padova, Italy
[47] Dipartimento di Fisica, Università degli Studi di Roma "Tor Vergata", Via della Ricerca Scientifica 1, I-00133 Roma, Italy
[48] Department of Astronomy, University of Maryland, College Park, MD 20742, USA
[49] Anton Pannekoek Institute for Astronomy & GRAPPA, University of Amsterdam, Science Park 904, 1098 XH Amsterdam, The Netherlands
[50] Guangxi Key Laboratory for Relativistic Astrophysics, School of Physical Science and Technology, Guangxi University, Nanning 530004, People's Republic of China
Received 2022 August 30; revised 2022 December 19; accepted 2022 December 21; published 2023 February 2

Abstract

The launch of the Imaging X-ray Polarimetry Explorer (IXPE) on 2021 December 9 has opened a new window in X-ray astronomy. We report here the results of the first IXPE observation of a weakly magnetized neutron star, GS 1826−238, performed on 2022 March 29–31 when the source was in a high soft state. An upper limit (99.73% confidence level) of 1.3% for the linear polarization degree is obtained over the IXPE 2–8 keV energy range. Coordinated INTEGRAL and NICER observations were carried out simultaneously with IXPE. The spectral parameters obtained from the fits to the broadband spectrum were used as inputs for Monte Carlo simulations considering different possible geometries of the X-ray emitting region. Comparing the IXPE upper limit with these simulations, we can put constraints on the geometry and inclination angle of GS 1826–238.

Unified Astronomy Thesaurus concepts: Low-mass x-ray binary stars (939); X-ray astronomy (1810); X-ray binary stars (1811)

1. Introduction

Weakly magnetized neutron stars in low-mass X-ray binaries (NS-LMXBs) are believed to accrete via Roche-lobe overflow from a stellar companion, which is typically a main-sequence star with a mass lower than $\sim 1\,M_{\odot}$ or an evolved white dwarf. These objects are highly variable in the X-ray at a timescale ranging from milliseconds to years. The classification of NS-LMXBs is historically based on the tracks that they draw on the so-called color–color diagram (CCD; Hasinger & van der Klis 1989; van der Klis 1995). The sources are divided as a function of the X-ray luminosity as follows: (a) high soft state (HSS) Z sources ($>10^{38}$ erg s^{-1}), (b) HSS bright atoll sources ($10^{37}-10^{38}$ erg s^{-1}), and (c) low hard state (LHS) atoll sources ($\sim 10^{36}$ erg s^{-1}; van der Klis 2006, and references therein). The "Z" and "atoll" terms directly derive from the shape of the track in the CCDs. The majority of persistent NS-LMXBs are generally observed either in HSS or (less frequently) in LHS, but most of the transients and several persistent sources can perform state transitions from LHS to HSS and vice versa in a relatively short timescale (van der Klis 2006).

The emission of this class of sources consists of two main spectral components: a soft (<1 keV) thermal component produced by a relatively cold, optically thick accretion disk and a hard component that can be modeled with Comptonization in a hot, relatively optically thin electron plasma (often called a corona; Done et al. 2007). Moreover, the frequent observation of an iron emission line at ∼6–7 keV, especially in the HSS sources (Ludlam et al. 2022), is likely a signature of reflection by a colder medium (such as the geometrically thin accretion disk itself). In addition, the HSS spectra could show transient hard tails detected well beyond the Comptonized component and up to ∼200–300 keV whose origin is unclear (see Paizis et al. 2006, and references therein). In LHS (but rarely also in HSS), NS-LMXBs typically show X-ray bursts, which are occasional powerful flashes (with a fluence of $\sim 10^{40}$ erg on an ∼100 s timescale) due to a thermonuclear runaway in the dense H+He layer at the NS surface (Lewin et al. 1993). The evolution of the physical parameters (plasma temperature, accretion rate, inner disk radius, etc.) defines the characteristics of the spectral states. For example, LHS plasma is much hotter and transparent (electron temperature $kT > 20$ keV, Thomson optical depth $\tau \sim 2$) with respect to the HSS ones ($kT \sim 3$ keV, $\tau > 5$, depending on the geometry of the plasma itself).

The presence of the NS surface stops the accretion flow, forming a transition layer between the disk and the NS surface. This layer is also named the spreading (SL) or boundary (BL) layer. In particular, the BL is the part of the accretion disk where the gas decelerates, while the SL is the gas layer at the NS surface, which can extend to high latitudes (Inogamov & Sunyaev 1999; Suleimanov & Poutanen 2006). In one of the most accredited models, the Eastern model (Mitsuda et al. 1984), the soft component originates in the accretion disk, while the electron corona Comptonizes the seed photons emitted by the NS surface and/or the BL/SL. Recently, Long et al. (2022) published a significant detection of a polarization signal (in the energy range 4–8 keV) in Sco X-1 with the PolarLight (Feng et al. 2019) instrument. Their results, in particular the polarization angle (PA) roughly aligned with the radio jet, favor an electron corona located in the SL/transition layer. Timing analysis of these sources also supports the presence of the SL, which may even be directly responsible for the emission of the hard component (Gilfanov et al. 2003; Revnivtsev & Gilfanov 2006). As discussed in Revnivtsev et al. (2013), on the basis of the RXTE data, the hard component of NS-LMXB spectra can be modeled with a diluted blackbody. However, high-sensitivity spectroscopy together with broad spectral coverage, such as that permitted by BeppoSAX or NuSTAR, has shown that the hard emission is compatible with a Comptonization spectrum (see, e.g., Di Salvo et al. 2002; Iaria et al. 2020, and references therein), rather than a diluted blackbody. Therefore, the nature of the hard component in the NS-LMXB spectra still remains an unresolved issue. In this framework, spectroscopy cannot help because of degeneracy in the parameter space providing information on the shape and extension of the region where

[51] Deceased.

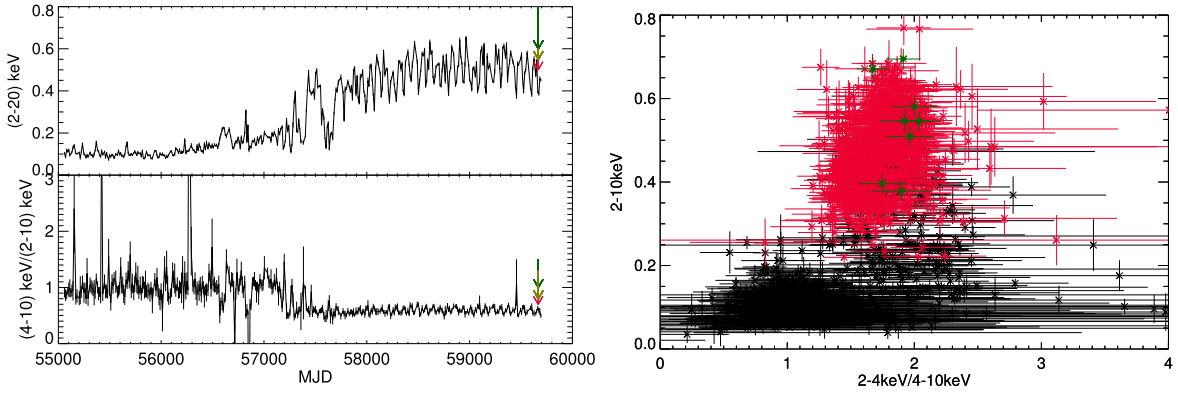

Figure 1. Top left panel: 2–20 keV MAXI light curve of GS 1826–238 in units of ph cm^{-2} s^{-1}. Bottom left panel: HR (2–4 keV/4–10 keV) as a function of time. The green, gray, and red arrows indicate the IXPE, NICER, and INTEGRAL observation dates, respectively. Right panel: HID of GS 1826–238 derived from the MAXI data. The red points correspond to the HSS after the major transition in MJD 57,500 (the black points represent the HID before MJD 57,500), while the green points correspond to the times of the NICER, IXPE, and INTEGRAL/JEM-X observations reported in this paper. Flux variations among the green points are mostly due to the MAXI spurious modulation (Mihara et al. 2022).

Comptonization occurs. Polarimetry is the key to identify the nature and geometry of the system removing degeneracy left by spectroscopy. In fact, different geometries and viewing angles result in quite different polarization degrees (PDs) and PAs.

1.1. GS 1826–238

Object GS 1826–238 is an accreting NS-LMXB. Until 2016, it was classified as an atoll source in the hard spectral state. A peculiarity of this source was the presence of extremely regular X-ray bursts over a range of several years (Cocchi et al. 2000; Zamfir et al. 2012). For this reason, it is also known as a "clocked burster." The clocked bursts occurred when GS 1826–238 was in the hard state, as indicated by the CCD (Cocchi et al. 2011; Sánchez-Fernández et al. 2020), while during the occasional short transitions to the HSS (happened before MJD 57,500), the bursts occurred less regularly and were often shorter than in the hard state (Chenevez et al. 2016). At the beginning of 2016, GS 1826–238 underwent a major transition to the HSS. After that, the source remained in the same state until the observational campaign described in this paper. The characteristics of the GS 1826–238 binary system are poorly known. As reported by Homer et al. (1998), a low-amplitude modulation present in the optical light curve and the lack of eclipses imply a probable inclination of less than 70°. Other authors reported tighter constraints. For example, Johnston et al. (2020) modeled multiepoch X-ray bursts from GS 1826–238 with Markov Chain Monte Carlo simulations, obtaining an inclination angle of $i \sim 69^{+2}_{-3}$° (see also Dohi et al. 2020). Mescheryakov et al. (2011) estimated an inclination angle of $62.^{\circ}5 \pm 5.^{\circ}5$ from the mean optical flux and the amplitude of periodic modulations in the optical light curve.

2. Data Reduction and Analysis

2.1. The Long Time Behavior of GS 1826–238

The top left panel of Figure 1 reports the 2–10 keV MAXI (Matsuoka et al. 2009) light curve of GS 1826–238, while the bottom left panel shows the hardness ratio (HR). The major transition of GS 1826–238 to the HSS is clearly visible in the MAXI light curve and the HR at about MJD 57,500. After that date, the large and periodic ($P \sim 72$ days) flux variations correspond to only slight variations in the HR (left panels of Figure 1), probably due to a spurious 72 day oscillation sometimes present in the MAXI light curves (Mihara et al. 2022). The right panel of Figure 1 shows the hardness–intensity diagram (HID) for the sources based on the MAXI data.[52] The red points represent the values of the HID after the major transition to HSS and are all concentrated in a narrow range of intensity and hardness. This implies that, after MJD 57,500, there were no transitions back to LHS. On the contrary, the spreading of the black points is due to several short transitions to the HSS before MJD 57,500.

Table 1
IXPE, NICER, and INTEGRAL Observation Log

Telescope	ObsID	Date	Net Exposure (ks)
IXPE	01002801	2022-3-29/31	92
NICER	5050310103	2022-3-30	6.4
INTEGRAL	2485/1970005	2022-3-28/30	139/108[a]

Note.
[a] JEM-X1/JEM-X2 exposure time.

The Imaging X-ray Polarimetry Explorer (IXPE) observed the source on 2022 March 29–31. A coordinated observational campaign with NICER and INTEGRAL was performed simultaneously with IXPE. The dates and the duration of the observations are reported in Table 1. An X-ray burst was detected in the JEM-X data in a time period not overlapping with NICER and IXPE observations (MJD 59,667). The science window containing the X-ray burst (ID: 248500190010) was excluded from data analysis. The green points in Figure 1 represent the values of HID at the time of the IXPE, NICER, and INTEGRAL observations.

2.2. IXPE Data

The IXPE (Weisskopf et al. 2022) is a NASA/ASI mission launched on 2021 December 9. It is observing all major classes of galactic and extragalactic X-ray sources, providing space-, energy-, and time-resolved polarimetry (Soffitta et al. 2021). With respect to the previous X-ray polarimetric mission, OSO-8, IXPE needs about 2 orders of magnitude less exposure time to reach the same sensitivity, and it provides imaging capability

[52] Here we report the HID and not the CCD for the GS 1826–238 MAXI data because the errors in the CCD are too large to obtain a clear diagram.

with $\leqslant 30''$ angular resolution over $>11'$ field of view, together with 1–2 μs timing accuracy and a moderate spectral resolution typical for proportional counters. It consists of three X-ray telescopes with identical mirror modules and polarization-sensitive imaging detector units (DUs) at their focus. The IXPE observation took place on 2022 March 29–31 for a total net exposure time of 85 ks after taking into account Earth occultations.

The IXPE data extraction was performed by means of the IXPE collaboration software tool IXPEOBSSIM (Baldini et al. 2022) version 26.3.2, with `xppicorr` to apply the energy calibration with in-flight calibration sources (as such, a correction was not yet implemented in the official pipeline at the time of the observation), `xpselect` to filter data, and `xpbin` to apply different binning algorithms for generating images and spectra. Rebinning and spectropolarimetric analysis was performed with FTOOLS and XSPEC (HEASOFT version 6.30.1). We compared the results of the polarimetric analysis obtained with both XSPEC and IXPEOBSSIM tools (`pcube`). While XSPEC requires the definition of a spectropolarimetric model, IXPEOBSSIM allows a model-independent analysis that computes the polarization only on the basis of detected photons. The IXPEOBSSIM response matrices version v010 were employed, corresponding to the latest available version in the HEASARC database. Data analysis was performed following the unweighted method.[53]

The statistical uncertainties of PD and PA when using IXPEOBSSIM are calculated with the assumption that the Stokes parameters are normally distributed and uncorrelated, and that PD and PA are considered independent, as described in Kislat et al. (2015). We report these uncertainties in the tables as a 68.27% (1σ) confidence level. The uncertainties from the XSPEC analysis reported in the tables are computed with the `error` command of XSPEC for one parameter of interest.

It is worth noting that the PD and PA are not actually independent. The contours representing the 68.27%, 95.45%, and 99.73% confidence levels of the joint measurement of the PD and PA are a more appropriate method to represent the uncertainties. With IXPEOBSSIM, such contours are derived as described in Weisskopf et al. (2010), Strohmayer & Kallman (2013), and Muleri (2022) by using the parameters obtained by the `pcube` algorithm itself. In XSPEC, the contours are obtained using the `steppar` command for two parameters of interest. The upper limits to the PD are based upon its error in one dimension, without regard to the value of the PA. Therefore, they are computed using a χ^2 with one degree of freedom.

Source and background regions were selected from the image of each DU. The source is centered on a circular region of $60''$ in radius. The background is extracted from an annular region with internal and external radii of $180''$ and $240''$, respectively. The background is almost negligible with respect to the source. The ratio of counts of background over the source (by scaling for the extraction region areas) is only $\sim$0.3%.

2.2.1. The IXPE Spectrum

The IXPE light curve and HR are substantially constant, so we extracted the nine IXPE Stokes parameters (I, Q, and U for each DU), integrating over the entire observation. However, it should be noted that they were not compatible with the NICER +JEM-X spectra due to an improper correction of telescope vignetting caused by the off-axis pointing of GS 1826–238 still present on the date of the observation. Due to GS 1826–238's brightness, the systematic effect induced is highly significant in the energy spectrum.[54] It must be remarked, however, that this problem affects I, Q, and U in the same way; therefore, the PD and PA are not affected.

2.3. NICER Data

NICER performed four observations of the source with continuous exposure in the period 2022 March 28–31. During the first two observations, significant variability in the HR did not permit extraction of a single averaged spectrum. For this reason, we used in the joint fit only the third observation, ObsID 5050310103, which was simultaneous with IXPE and has an exposure time of 6.4 ks. The NICER data were reduced using HEASOFT 6.30 and the NICERL2 task to apply standard calibration and screenings with CALDB version 20210707.

2.4. INTEGRAL Data

INTEGRAL observed the source from 2022 March 28 17:25 to 2022 March 30 23:40 UT for a total of 186 ks. INTEGRAL data were reduced using the latest release of the standard Online Scientific Analysis (version 11.2), distributed by the INTEGRAL Science Data Centre (Courvoisier et al. 2003) through the multimessenger online data analysis platform (Neronov et al. 2021). These target-of-opportunity observations were performed using hexagonal dithering to maintain GS 1826–238 in the fully coded field of view of JEM-X, the INTEGRAL X-ray telescope (Lund et al. 2003). The JEM-X spectra were extracted in the range 3–35 keV with a response matrix with 16 standard channels. A systematic error of 1.5% was added in quadrature for the spectral analysis. Even if the INTEGRAL observation did not exactly overlap the IXPE and NICER observations, the JEM-X spectrum was in good agreement with the NICER one. Because the JEM-X HR did not change significantly during the observation, it was possible to extract the averaged spectrum. Only the JEM-X data were used for the spectral extraction because IBIS, the γ-ray energy detector (Ubertini et al. 1999; Lebrun et al. 2003), did not detect the source with a 3σ upper limit on the flux of $\sim 10^{-11}$ erg cm^{-2} s^{-1} (3 mCrab) in the 28–40 keV energy range, implying that the high-energy tail was not present.

3. Results

3.1. Spectroscopy of GS 1826–238

We carried out the spectral analysis of the joint NICER and JEM-X spectrum using XSPEC version 12.12.1. The model used for the fitting procedure is a disk blackbody component (Mitsuda et al. 1984) plus a Comptonization of soft photons in a hot plasma (Titarchuk 1994). Both components are modified by interstellar absorption. The XSPEC syntax of the model has the form `phabs*(diskbb+comptt)`. No reflection component or iron line are needed in the spectral fit. We performed the spectral fitting for two different geometries: slab and sphere. The spectral parameters obtained from the fitting

[53] In the unweighted analysis method, equal weights are assigned to each photoelectron track, regardless of its shape.

[54] https://heasarc.gsfc.nasa.gov/FTP/ixpe/data/obs/01/01002801/README

Table 2
Best-fit Spectral Parameters Obtained from the NICER and JEM-X Data

Fit Parameter	Slab/Sphere
$N_{\rm H}$ (10^{22} cm^{-2})[a]	$0.351^{+0.004}_{-0.005}$
$kT_{\rm in}$ (keV)[b]	0.94 ± 0.1
$N_{\rm d}$ ($R_{\rm in}$ km)[c]	$277^{+134}_{-55}(14^{+3}_{-2})$
kT_0 (keV)[d]	1.3 ± 0.2
$kT_{\rm e}$ (keV)[e]	$2.7^{+3.0}_{-0.2}$
$\tau_{0,\rm slab}$ ($\tau_{0,\rm sphere}$)[f]	$4.9^{+1.8}_{-3.2}$ $(10.8^{+3.5}_{-6.8})$
$N_{\rm C}$[g]	0.3 ± 0.1
$\chi^2_{\rm red}$ (d.o.f.)[h]	0.7 (172)
$f_{(2-8\ \rm keV)}$ (erg cm^{-2} s^{-1})[i]	4.42×10^{-9}
$f_{(2-4\ \rm keV)}$ (erg cm^{-2} s^{-1})[i]	2.24×10^{-9}
$f_{(4-8\ \rm keV)}$ (erg cm^{-2} s^{-1})[i]	2.18×10^{-9}
$f^{\rm ph}_{\rm disk}/f^{\rm ph}_{\rm tot}$[j]	0.55
$f^{\rm ene}_{\rm disk}/f^{\rm ene}_{\rm tot}$[k]	0.45

Notes. Both slab and sphere geometries give identical spectral parameters, except for the value of plasma optical depth.
[a] Equivalent hydrogen column density.
[b] Inner disk temperature.
[c] The diskbb normalization parameter $N_{\rm d} = (R_{\rm in}/10\ {\rm kpc})^2 \cos\theta$, where $R_{\rm in}$ is the disk inner radius in kilometers, and θ is the viewing angle ($\theta = 60°$).
[d] Seed photon temperature.
[e] Electron temperature.
[f] Plasma optical depths for spherical and slab geometry.
[g] Normalization of the comptt component.
[h] Reduced χ^2 and degrees of freedom.
[i] The unabsorbed flux in the energy range specified by the subscript.
[j] Fraction of all photons in the 2–8 keV range in the diskbb component.
[k] Fraction of the energy flux in the 2–8 keV in the diskbb component.

procedures are reported in Table 2. The corresponding unfolded spectrum is shown in Figure 2. The features present in the residuals are due to NICER instrumental issues (Miller et al. 2018; Strohmayer et al. 2018). We verified in two different ways that these features do not affect the continuous spectrum: (1) modeling the features by adding two Gaussian line profiles to the model and (2) ignoring the NICER spectrum in the range 0–2.3 keV. In both cases, the spectral parameters remain consistent within the errors.

The spectrum of GS 1826–238 is consistent with those reported in the literature for a weakly magnetized NS-LMXB in HSS, with a low temperature (∼2.7 keV) and a highly opaque electron plasma (see, for example, Paizis et al. 2006). As expected, both geometries are consistent with the data (see Table 2 for details).

3.2. Polarization Measurements

The Stokes parameters of GS 1826–238 observed by IXPE in the 2–8, 2–4, and 4–8 keV energy bands, obtained with IXPEOBSSIM, are reported in Table 3 and Figure 3. No detection of polarization can be claimed. We also analyzed the variation of Stokes parameters as a function of time, but we did not obtain any significant detection.

We performed the fitting spectropolarimetric procedure by applying the POLCONST convolution model to the IXPE spectra (I, Q, and U) using XSPEC (syntax: polconst*phabs (diskbb+comptt)). This model describes a constant source polarization. In order to derive the polarization parameters (PD and PA of the polconst model), the spectral parameters of the phabs, diskbb, and comptt models were fixed to those

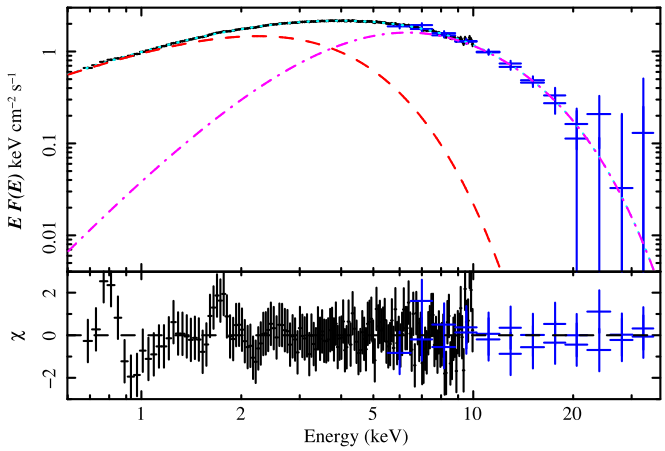

Figure 2. Unfolded spectrum of GS 1826–238 as observed by NICER (black crosses) and JEM-X1 and 2 (blue crosses). The red dashed line represents the accretion disk emission (diskbb in XSPEC); the pink dotted–dashed line represents the emission of the Comptonized component (comptt in XSPEC). The spectral parameters are given in Table 2. The residuals below 2 keV are due to the NICER instrumental issue as reported by Miller et al. (2018) and do not significantly affect the continuous spectrum (see text for details).

Table 3
Normalized Stokes Parameters for GS 1826–238 as Observed by the Three DUs of IXPE in Various Energy Bands

	DU1	DU2	DU3	All DUs
		2–8 keV		
Q/I (%)	-0.48 ± 0.63	-0.14 ± 0.65	-0.11 ± 0.66	0.18 ± 0.37
U/I (%)	-0.90 ± 0.63	-0.49 ± 0.65	-0.90 ± 0.66	0.42 ± 0.37
		2–4 keV		
Q/I (%)	-0.50 ± 0.62	-0.23 ± 0.63	-0.26 ± 0.65	0.17 ± 0.37
U/I (%)	-1.42 ± 0.62	-0.28 ± 0.63	-0.16 ± 0.65	0.45 ± 0.37
		4–8 keV		
Q/I (%)	-0.4 ± 1.3	-0.1 ± 1.3	-0.2 ± 1.3	0.19 ± 0.74
U/I (%)	-0.3 ± 1.3	-1.0 ± 1.3	-2.7 ± 1.3	0.37 ± 0.74

Note. The values of the average modulation factors of the three DUs in various energy ranges are 31.8% (2–8 keV), 26.7% (2–4 keV), and 43.6% (4–8 keV).

found from spectral fitting of the NICER and JEM-X data (see Table 2). As expected, the PD is compatible with null polarization, and the PA is unconstrained even at a confidence level as low as 68.27%. Table 4 reports the upper limits calculated with both IXPEOBSSIM and XSPEC at different confidence levels.

Figure 4 reports the contours of the PD and PA of the IXPE observation in the 2–8, 2–4, and 4–8 keV energy bands. They are obtained with both XSPEC (red cross and solid contours) and IXPEOBSSIM (pink star and dashed contours) by summing the events from the three DUs. The 1σ upper limits on the PD from IXPEOBSSIM (0.84%, 0.85%, and 0.94% in the 2–8, 2–4, and 4–8 keV range, respectively; see Table 4) derived as described in Baldini et al. (2022) are somewhat larger than the estimates using a Bayesian approach presented by Maier et al. (2014), which would give 0.56%, 0.59%, and 0.82%, but are consistent with the corresponding limits from XSPEC of 0.69%, 0.90%, and 0.82%. The XSPEC 3σ upper limits (99.73% confidence level) are 1.3%, 1.6%, and 2.0%, while the Bayesian approach gives rather consistent limits of 1.41%,

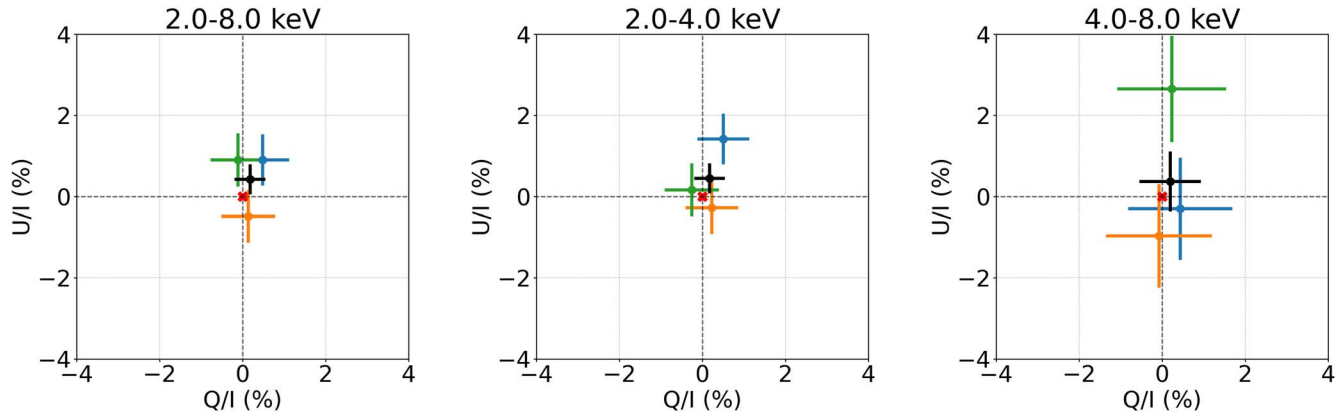

Figure 3. Stokes parameters in the 2–8, 2–4, and 4–8 keV energy band for DU1 (blue), DU2 (orange), and DU3 (green) and by summing the events of the three DUs (black). The red point represents the null polarization.

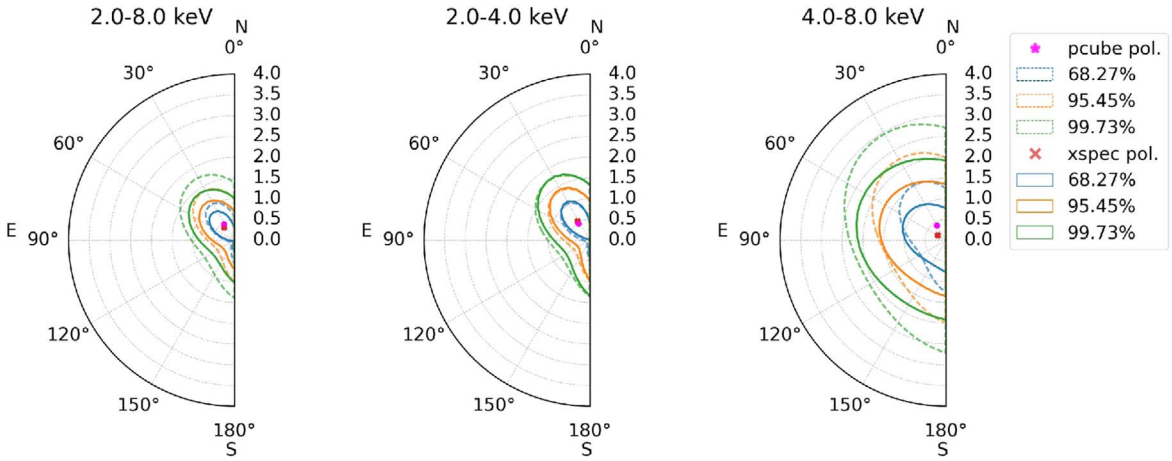

Figure 4. Contour of the PD and PA for GS 1826–238 in the 2–4, 4–8, and 2–8 keV energy bands obtained with XSPEC (red cross and solid contours) and IXPEOBSSIM (pink star and dashed contours) by summing the events from the three DUs. Contours correspond to the 68.27%, 95.45%, and 99.73% confidence levels. Both sets of contour levels, obtained with XSPEC and IXPEOBSSIM, are computed for a joint measurement of PD and PA. Therefore, they are derived using a χ^2 with two degrees of freedom.

1.44%, and 2.37%. In any case, the PA is unconstrained in all three energy bands (see Figure 4).

4. Discussion and Conclusions

In order to put constraints on the geometry of the GS 1826–238 system, we first performed simulations with the general relativistic Monte Carlo code, MONK (Zhang et al. 2019), suitably adapted to compute the X-ray polarized radiation coming from weakly magnetized NS-LMXBs in Kerr spacetime, accounting for the contributions of the NS, disk, and corona (for details, see Gnarini et al. 2022, and references therein).

As reported in Gnarini et al. (2022), a blackbody spectrum is assumed to model the unpolarized NS surface emission, while the seed photons from the disk are generated according to the disk emissivity. The hot electron corona is illuminated by both the NS and the accretion disk, and, when a photon reaches the corona, it is Compton scattered, assuming the Klein–Nishina cross section. The energy and polarization spectrum is produced by counting the photons that arrived at the observer.

The simulations were performed using as input parameters the best-fit spectral parameters reported in Table 2 for different geometries and considering a standard NS with 1.4 $M_\odot$, a 12 km radius, and a 3 ms period, in analogy to the one derived

Table 4
X-Ray Polarization of GS 1826–238 Computed by Means of IXPEOBSSIM and XSPEC

Energy Band		PD (%)
2–8 keV		
	IXPEOBSSIM @68.27% (1σ)	<0.84
	XSPEC @68.27%	<0.69
	XSPEC @99.73%	<1.3
2–4 keV		
	IXPEOBSSIM @68.27% (1σ)	<0.85
	XSPEC @68.27%	< 0.90
	XSPEC @99.73%	<1.6
4–8 keV		
	IXPEOBSSIM @68.27% (1σ)	<0.94
	XSPEC @68.27%	<0.82
	XSPEC @99.73%	<2.0

Note. The IXPEOBSSIM uncertainties are estimated assuming that variables are normally distributed, whereas XSPEC uncertainties are estimated by varying each parameter along the χ^2 surface. The upper limits to the PD are obtained from the one-dimensional errors, without regard to the value of the PA. Thus, they are computed using a χ^2 with one degree of freedom.

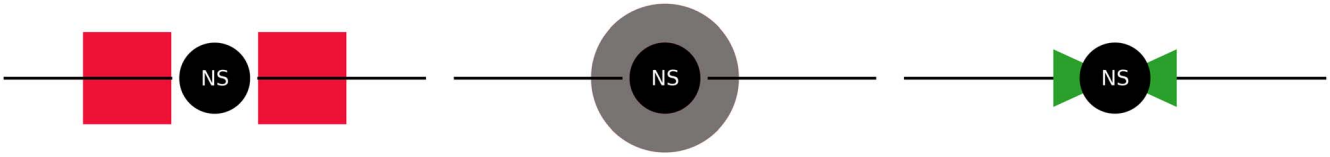

Figure 5. Schematic representation of the three different geometries used in MONK simulations: the pseudotoroidal geometry (left panel), the shell (middle panel), and the wedge (right panel).

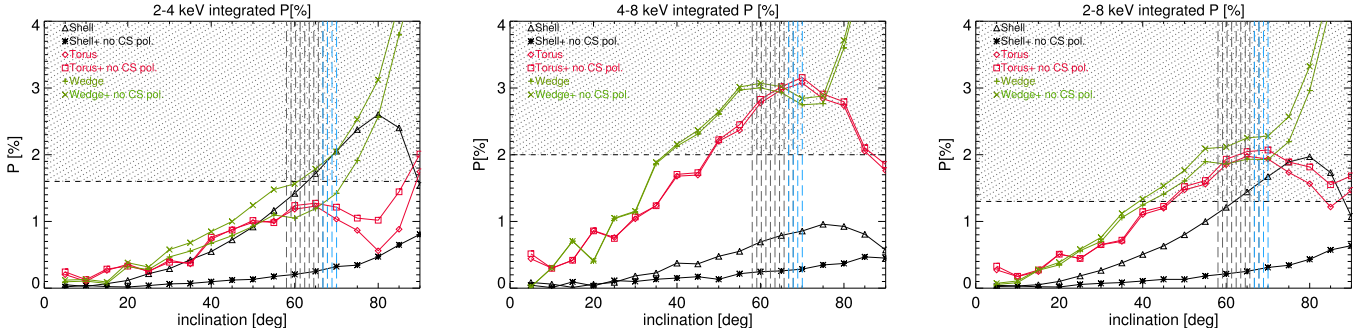

Figure 6. MONK simulations of GS 1826–238 PD integrated over different energy ranges, 2–4 (left panel), 4–8 (middle panel), and 2–8 (right panel) keV, as a function of the inclination angle. The black horizontal dashed lines represent the upper limits on the PD from Table 4. The upper gray hatched regions represent the values of PD excluded by our results, while the vertical dashed bands represent the interval of i fixed by the indirect measurements of the GS 1826–238 inclination angle reported by both Johnston et al. (2020, black dashed lines) and Mescheryakov et al. (2011, light blue dashed lines). Results are given for two cases of disk seed photons: polarized according to the Chandrasekhar (1960) law or unpolarized (labeled "no CS pol").

from QPOs by Wijnands et al. (1998) for Cygnus X-2 (see also Patruno et al. 2017, for a statistical analysis of the spin distributions of NS-LMXBs). In order to prove the presence, and eventually the geometry, of the electron corona and test if the nature of the hard component is instead strictly connected with the SL, we performed simulations with three different geometries, chosen among those implemented in the code, as shown in Figure 5.

1. Pseudotoroidal geometry (as defined in Gnarini et al. 2022): a rectangular section torus with similar vertical and horizontal length scales ($2H \sim \Delta R$) corotating with the disk. As reported in Gnarini et al. (2022), the slab corona is assumed to cover only part of the disk, starting from the inner disk radius until 15 gravitational radii, while the vertical thickness is set in order to cover most of the NS surface.
2. Shell geometry: a stationary spherical shell surrounding the NS (roughly mimicking the SL of Inogamov & Sunyaev 1999). We chose the same radius used in Gnarini et al. (2022).[55] However, when varying the radius of the shell, the symmetry does not change; consequently, the PD remains substantially unvaried.
3. Wedge geometry: a conical section torus around the NS equator lying between the disk and the NS surface and rotating with Keplerian velocity (roughly mimicking the equatorial BL; e.g., Popham & Sunyaev 2001). The torus is joined to both the NS surface and the inner part of the disk (it extends from 6 to 8 gravitational radii).

Figure 6 shows the net polarization fraction integrated over three different IXPE energy bands as a function of the inclination angle for the three different geometries. We also consider two cases for the polarization of the disk seed photons: polarized according to the Chandrasekhar (1960) law for the semi-infinite, plane-parallel, pure electron-scattering atmosphere, and unpolarized (labeled "no CS pol" in Figure 6). The black dashed lines represent the IXPE 3σ upper limit for each energy band (see Table 4).

For the pseudotoroidal geometry, the presence of the intrinsic polarization of disk seed photons does not significantly change the net fraction of polarized light, since disk photons dominate only at lower energies. Therefore, we can derive a relatively stringent upper limit on the viewing angle: $i \lesssim 47°$ (see the right panel of Figure 6). The PA for the pseudotoroidal geometry is misaligned and not perpendicular with respect to the disk as a result of the sum of the disk and NS contributions together with general relativity (GR) effects (see Gnarini et al. 2022, for more details on this geometry).

Considering the shell geometry, the presence or absence of intrinsic polarization could substantially change the PD, while the PA is always parallel to the disk. In fact, for unpolarized disk seed photons, the fraction of polarized light remains well below 1% for all inclinations in all energy bands. On the other hand, in the case of intrinsic polarization of the seed photons, a constraint on the GS 1826–238 viewing angle is derived: $i \lesssim 62°$ (see left panel of Figure 6).

Finally, for the wedge geometry, the presence or absence of intrinsic polarization slightly changes the polarization fraction, giving upper limits of $i \lesssim 42°$ and 39°, respectively. For this configuration, the PA is misaligned by approximately 25° from the projection of the rotation axis as a result of general and special relativity effects and the sum of the different photon populations.

On the other hand, comparing the inclination values reported by previous authors, i.e., $69^{+2}_{-3}°$ (Johnston et al. 2020) and $62.^{\circ}5 \pm 5.^{\circ}5$ (Mescheryakov et al. 2011), with our simulations, both the pseudotoroidal and wedge geometries seem to be excluded. In fact, as the plots in Figure 6 show, for inclinations between 57° and 72°, there should be a detection of polarization in at least one of the three considered energy ranges (see the regio blue and black dashed lines in the three

[55] Some preliminary tests on a corotating corona indicate that the PD is similar to the stationary case.

panels of Figure 6). For the shell geometry and no intrinsic polarization, there is no detection within the interval of viewing angles considered in all three energy ranges. On the contrary, in the case of shell geometry and intrinsic polarization, the interval of the viewing angles with no detection is restricted to $57^\circ \lesssim i \lesssim 62^\circ$, excluding the values of inclination reported by Johnston et al. (2020), $i \sim 69^{+2}_{-3}{}^\circ$ but not those reported by Mescheryakov et al. (2011), $i \sim 62.^\circ5 \pm 5.^\circ5$. However, the results are computed using only the value of the best-fit parameters without including the errors. These can lead to slight variations on the inclination constraints. Therefore, either the GS 1826–238 system could have a spherical symmetry, or its inclination is lower than previously measured. In fact, most of the simulations show (see, e.g., Schnittman & Krolik 2009; Gnarini et al. 2022) that small viewing angles correspond to a lower fraction of polarized light emitted by a source.

We have to underline that a significant percentage of polarized light was measured in various LMXBs, such as the mentioned Sco X-1 and, recently, Cyg X-2 (Farinelli et al., submitted). Both sources are observed at inclination angles comparable with that of GS 1826–238. However, these two sources are classified as Z sources, while GS 1826–238 is the first atoll source observed by IXPE. A comparison between the two kinds of sources is not always possible. For example, Long et al. (2022) reported that in Sco X-1, the PD has a strong dependence on the luminosity and the spectral branch. Instead, the IXPE data of GS 1826–238 present a quite stable light curve and HR. Therefore, it is impossible to extract any information about the evolution of the PD as a function of luminosity and the spectral state, unlike the case of Sco X-1.

As reported by Lapidus & Sunyaev (1985) and Schnittman & Krolik (2009), the reflection from the accretion disk of the radiation produced by the SL or self-illumination of the disk can produce substantial polarization. However, in GS 1826–238, we do not detect, at least with the spectral resolution of NICER, the iron line that is a typical signature of disk reflection in the HSS sources (e.g., Cyg X-2 and Sco X-1; Di Salvo et al. 2002; D'Aí et al. 2007). One possibility is that the disk is strongly ionized, reducing the strength of the iron line. On the other hand, the latitudinal extent of the SL might not be large enough to produce significant illumination of the disk, resulting in a weak signal. This could be one of the reasons why we could only establish an upper limit for polarization in GS 1826–238.

Finally, by significantly varying the dimension of the hot corona or considering more complicated shapes (e.g., a combination of two proposed geometries), the PD could be very different compared to the previous cases. However, if we assume that the spherical geometry that seems favored by the simulations mimics the SL (and thus the SL subsumes the role of the corona), it could not be extended more than some fraction of the NS radius (the same line of thinking could be applied in the case of the BL). Furthermore, two different emission components (for example, the disk and the reflection component) or two different populations of electrons emitting in different regions may have a similar PD but an orthogonal PA.

The Imaging X-ray Polarimetry Explorer (IXPE) is a joint US and Italian mission. The US contribution is supported by the National Aeronautics and Space Administration (NASA) and led and managed by its Marshall Space Flight Center (MSFC), with industry partner Ball Aerospace (contract NNM15AA18C). The Italian contribution is supported by the Italian Space Agency (Agenzia Spaziale Italiana, ASI) through contract ASI-OHBI-2017-12-I.0, agreements ASI-INAF-2017-12-H0 and ASI-INFN-2017.13-H0, and its Space Science Data Center (SSDC) with agreements ASI-INAF-2022-14-HH.0 and ASI-INFN 2021-43-HH.0, and by the Istituto Nazionale di Astrofisica (INAF) and the Istituto Nazionale di Fisica Nucleare (INFN) in Italy.

This research used data products provided by the IXPE Team (MSFC, SSDC, INAF, and INFN) and distributed with additional software tools by the High-Energy Astrophysics Science Archive Research Center (HEASARC) at NASA Goddard Space Flight Center (GSFC). This work made use of the MAXI light curves, publicly available at http://maxi.riken.jp/top/slist.html. INTEGRAL is an ESA project with instruments and a science data center funded by ESA member states (especially the PI countries: Denmark, France, Germany, Italy, Switzerland, and Spain) and with the participation of Russia and the USA. We thank Keith Gendreau, Craig Markwardt, and the NICER SOC for granting and performing the NICER observations of the source and helping with data reduction.

J.P. and S.S.T. acknowledge support from Russian Science Foundation grant 20-12-00364 and Academy of Finland travel grants 349144, 349373, and 349906. J.P. and J.J.E.K. were supported by Academy of Finland grant 333112.

Facilities: IXPE, Swift (XRT and UVOT), INTEGRAL.

Software: Stingray (Huppenkothen et al. 2019a, 2019b), XSPEC (Arnaud 1996), IXPEOBSSIM (Baldini et al. 2022), MONK (Zhang et al. 2019).

ORCID iDs

Fiamma Capitanio https://orcid.org/0000-0002-6384-3027
Sergio Fabiani https://orcid.org/0000-0003-1533-0283
Andrea Gnarini https://orcid.org/0000-0002-0642-1135
Francesco Ursini https://orcid.org/0000-0001-9442-7897
Carlo Ferrigno https://orcid.org/0000-0003-1429-1059
Giorgio Matt https://orcid.org/0000-0002-2152-0916
Juri Poutanen https://orcid.org/0000-0002-0983-0049
Massimo Cocchi https://orcid.org/0000-0002-5817-3129
Romana Mikusincova https://orcid.org/0000-0001-7374-843X
Ruben Farinelli https://orcid.org/0000-0003-2212-367X
Stefano Bianchi https://orcid.org/0000-0002-4622-4240
Jari J. E. Kajava https://orcid.org/0000-0002-3010-8333
Fabio Muleri https://orcid.org/0000-0003-3331-3794
Celia Sanchez-Fernandez https://orcid.org/0000-0002-0778-6048
Paolo Soffitta https://orcid.org/0000-0002-7781-4104
Kinwah Wu https://orcid.org/0000-0002-7568-8765
Iván Agudo https://orcid.org/0000-0002-3777-6182
Lucio A. Antonelli https://orcid.org/0000-0002-5037-9034
Matteo Bachetti https://orcid.org/0000-0002-4576-9337
Luca Baldini https://orcid.org/0000-0002-9785-7726
Wayne H. Baumgartner https://orcid.org/0000-0002-5106-0463
Ronaldo Bellazzini https://orcid.org/0000-0002-2469-7063
Stephen D. Bongiorno https://orcid.org/0000-0002-0901-2097
Raffaella Bonino https://orcid.org/0000-0002-4264-1215
Alessandro Brez https://orcid.org/0000-0002-9460-1821
Niccolò Bucciantini https://orcid.org/0000-0002-8848-1392

Simone Castellano https://orcid.org/0000-0003-1111-4292
Elisabetta Cavazzuti https://orcid.org/0000-0001-7150-9638
Stefano Ciprini https://orcid.org/0000-0002-0712-2479
Enrico Costa https://orcid.org/0000-0003-4925-8523
Alessandra De Rosa https://orcid.org/0000-0001-5668-6863
Ettore Del Monte https://orcid.org/0000-0002-3013-6334
Laura Di Gesu https://orcid.org/0000-0002-5614-5028
Niccolò Di Lalla https://orcid.org/0000-0002-7574-1298
Alessandro Di Marco https://orcid.org/0000-0003-0331-3259
Immacolata Donnarumma https://orcid.org/0000-0002-4700-4549
Victor Doroshenko https://orcid.org/0000-0001-8162-1105
Michal Dovčiak https://orcid.org/0000-0003-0079-1239
Steven R. Ehlert https://orcid.org/0000-0003-4420-2838
Teruaki Enoto https://orcid.org/0000-0003-1244-3100
Yuri Evangelista https://orcid.org/0000-0001-6096-6710
Riccardo Ferrazzoli https://orcid.org/0000-0003-1074-8605
Javier A. Garcia https://orcid.org/0000-0003-3828-2448
Shuichi Gunji https://orcid.org/0000-0002-5881-2445
Jeremy Heyl https://orcid.org/0000-0001-9739-367X
Wataru Iwakiri https://orcid.org/0000-0002-0207-9010
Svetlana G. Jorstad https://orcid.org/0000-0001-6158-1708
Vladimir Karas https://orcid.org/0000-0002-5760-0459
Jeffery J. Kolodziejczak https://orcid.org/0000-0002-0110-6136
Henric Krawczynski https://orcid.org/0000-0002-1084-6507
Fabio La Monaca https://orcid.org/0000-0001-8916-4156
Luca Latronico https://orcid.org/0000-0002-0984-1856
Ioannis Liodakis https://orcid.org/0000-0001-9200-4006
Simone Maldera https://orcid.org/0000-0002-0698-4421
Alberto Manfreda https://orcid.org/0000-0002-0998-4953
Frédéric Marin https://orcid.org/0000-0003-4952-0835
Andrea Marinucci https://orcid.org/0000-0002-2055-4946
Alan P. Marscher https://orcid.org/0000-0001-7396-3332
Herman L. Marshall https://orcid.org/0000-0002-6492-1293
Tsunefumi Mizuno https://orcid.org/0000-0001-7263-0296
C.-Y. Ng https://orcid.org/0000-0002-5847-2612
Stephen L. O'Dell https://orcid.org/0000-0002-1868-8056
Nicola Omodei https://orcid.org/0000-0002-5448-7577
Chiara Oppedisano https://orcid.org/0000-0001-6194-4601
Alessandro Papitto https://orcid.org/0000-0001-6289-7413
George G. Pavlov https://orcid.org/0000-0002-7481-5259
Abel L. Peirson https://orcid.org/0000-0001-6292-1911
Matteo Perri https://orcid.org/0000-0003-3613-4409
Melissa Pesce-Rollins https://orcid.org/0000-0003-1790-8018
Pierre-Olivier Petrucci https://orcid.org/0000-0001-6061-3480
Maura Pilia https://orcid.org/0000-0001-7397-8091
Andrea Possenti https://orcid.org/0000-0001-5902-3731
Simonetta Puccetti https://orcid.org/0000-0002-2734-7835
Brian D. Ramsey https://orcid.org/0000-0003-1548-1524
John Rankin https://orcid.org/0000-0002-9774-0560
Ajay Ratheesh https://orcid.org/0000-0003-0411-4243
Roger W. Romani https://orcid.org/0000-0001-6711-3286
Carmelo Sgrò https://orcid.org/0000-0001-5676-6214
Patrick Slane https://orcid.org/0000-0002-6986-6756
Gloria Spandre https://orcid.org/0000-0003-0802-3453
Toru Tamagawa https://orcid.org/0000-0002-8801-6263
Fabrizio Tavecchio https://orcid.org/0000-0003-0256-0995
Roberto Taverna https://orcid.org/0000-0002-1768-618X
Allyn F. Tennant https://orcid.org/0000-0002-9443-6774
Nicholas E. Thomas https://orcid.org/0000-0003-0411-4606
Francesco Tombesi https://orcid.org/0000-0002-6562-8654
Alessio Trois https://orcid.org/0000-0002-3180-6002
Sergey S. Tsygankov https://orcid.org/0000-0002-9679-0793
Roberto Turolla https://orcid.org/0000-0003-3977-8760
Jacco Vink https://orcid.org/0000-0002-4708-4219
Martin C. Weisskopf https://orcid.org/0000-0002-5270-4240
Fei Xie https://orcid.org/0000-0002-0105-5826
Silvia Zane https://orcid.org/0000-0001-5326-880X

References

Arnaud, K. A. 1996, in ASP Conf. Ser. 101, Astronomical Data Analysis Software and Systems V, ed. G. H. Jacoby & J. Barnes (San Francisco, CA: ASP), 17
Baldini, L., Bucciantini, N., Di Lalla, N., et al. 2022, SoftX, 19, 101194
Chandrasekhar, S. 1960, Radiative Transfer (New York: Dover)
Chenevez, J., Galloway, D. K., in't Zand, J. J. M., et al. 2016, ApJ, 818, 135
Cocchi, M., Bazzano, A., & Natalucci, L. 2000, in AIP Conf. Ser. 510, The Fifth Compton Sym., American Inst. Phys. Conf. Ser, ed. M. L. McConnell & J. M. Ryan (Melville, NY: AIP), 203
Cocchi, M., Farinelli, R., & Paizis, A. 2011, A&A, 529, A155
Courvoisier, T. J. L., Walter, R., Beckmann, V., et al. 2003, A&A, 411, L53
D'Aí, A., Życki, P., Di Salvo, T., et al. 2007, ApJ, 667, 411
Di Salvo, T., Farinelli, R., Burderi, L., et al. 2002, A&A, 386, 535
Dohi, A., Hashimoto, M., Yamada, R., Matsuo, Y., & Fujimoto, M. Y. 2020, Progress of Theoretical and Experimental Physics, 2020, 3
Done, C., Gierliński, M., & Kubota, A. 2007, A&ARv, 15, 1
Feng, H., Jiang, W., Minuti, M., et al. 2019, ExA, 47, 225
Gilfanov, M., Revnivtsev, M., & Molkov, S. 2003, A&A, 410, 217
Gnarini, A., Ursini, F., Matt, G., et al. 2022, MNRAS, 514, 2561
Hasinger, G., & van der Klis, M. 1989, A&A, 225, 79
Homer, L., Charles, P. A., & O'Donoghue, D. 1998, MNRAS, 298, 497
Huppenkothen, D., Bachetti, M., Stevens, A. L., et al. 2019a, ApJ, 881, 39
Huppenkothen, D., Bachetti, M., Stevens, A., et al. 2019b, JOSS, 4, 1393
Iaria, R., Mazzola, S. M., Di Salvo, T., et al. 2020, A&A, 635, A209
Inogamov, N. A., & Sunyaev, R. A. 1999, AstL, 25, 269
Johnston, Z., Heger, A., & Galloway, D. K. 2020, MNRAS, 494, 4576
Kislat, F., Clark, B., Beilicke, M., & Krawczynski, H. 2015, APh, 68, 45
Lapidus, I. I., & Sunyaev, R. A. 1985, MNRAS, 217, 291
Lebrun, F., Leray, J. P., Lavocat, P., et al. 2003, A&A, 411, L141
Lewin, W. H. G., van Paradijs, J., & Taam, R. E. 1993, SSRv, 62, 223
Long, X., Feng, H., Li, H., et al. 2022, ApJL, 924, L13
Ludlam, R. M., Cackett, E. M., García, J. A., et al. 2022, ApJ, 927, 112
Lund, N., Budtz-Jørgensen, C., Westergaard, N. J., et al. 2003, A&A, 411, L231
Maier, D., Tenzer, C., & Santangelo, A. 2014, PASP, 126, 459
Matsuoka, M., Kawasaki, K., Ueno, S., et al. 2009, PASJ, 61, 999
Mescheryakov, A. V., Revnivtsev, M. G., & Filippova, E. V. 2011, AstL, 37, 826
Mihara, T., Tsunemi, H., & Negoro, H. 2022, in Handbook of X-ray and Gamma-ray Astrophysics, ed. C. Bambi & A. Santangelo (Singapore: Springer), in press
Miller, J. M., Gendreau, K., Ludlam, R. M., et al. 2018, ApJL, 860, L28
Mitsuda, K., Inoue, H., Koyama, K., et al. 1984, PASJ, 36, 741
Muleri, F. 2022, in Handbook of X-ray and Gamma-ray Astrophysics, ed. C. Bambi & A. Santangelo (Singapore: Springer), in press
Neronov, A., Savchenko, V., Tramacere, A., et al. 2021, A&A, 651, A97
Paizis, A., Farinelli, R., Titarchuk, L., et al. 2006, A&A, 459, 187
Patruno, A., Haskell, B., & Andersson, N. 2017, ApJ, 850, 106
Popham, R., & Sunyaev, R. 2001, ApJ, 547, 355

Revnivtsev, M. G., & Gilfanov, M. R. 2006, A&A, 453, 253
Revnivtsev, M. G., Suleimanov, V. F., & Poutanen, J. 2013, MNRAS, 434, 2355
Sánchez-Fernández, C., Kajava, J. J. E., Poutanen, J., Kuulkers, E., & Suleimanov, V. F. 2020, A&A, 634, A58
Schnittman, J. D., & Krolik, J. H. 2009, ApJ, 701, 1175
Soffitta, P., Baldini, L., Bellazzini, R., et al. 2021, AJ, 162, 208
Strohmayer, T. E., & Kallman, T. R. 2013, ApJ, 773, 103
Strohmayer, T. E., Gendreau, K. C., Altamirano, D., et al. 2018, ApJ, 865, 63
Suleimanov, V., & Poutanen, J. 2006, MNRAS, 369, 2036
Titarchuk, L. 1994, ApJ, 434, 570
Ubertini, P., Bazzano, A., Cocchi, M., et al. 1999, ApJL, 514, L27
van der Klis, M. 1995, in Cambridge Astrophysics Series, X-ray Binaries, Vol. 26, ed. W. Lewin, J. van Paradijs, & E. P. J. van den Heuvel (Cambridge: Cambridge Univ. Press), 252
van der Klis, M. 2006, in Cambridge Astrophysics Series, Compact stellar X-ray sources, Vol. 39, ed. W. Lewin & M. van der Klis (Cambridge: Cambridge Univ. Press), 39
Weisskopf, M. C., Elsner, R. F., & O'Dell, S. L. 2010, Proc. SPIE, 7732, 77320E 5
Weisskopf, M. C., Soffitta, P., Baldini, L., et al. 2022, JATIS, 8, 026002
Wijnands, R., Homan, J., van der Klis, M., et al. 1998, ApJL, 493, L87
Zamfir, M., Cumming, A., & Galloway, D. K. 2012, ApJ, 749, 69
Zhang, W., Dovčiak, M., & Bursa, M. 2019, ApJ, 875, 148